



## Research article

Zhiyuan Fan\*, Shourya Dutta-Gupta, Ran Gladstone, Simeon Trendafilov, Melissa Bosch, Minwoo Jung, Ganjigunte R. Swathi Iyer, Alexander J. Giles, Maxim Shcherbakov, Boris Feigelson, Joshua D. Caldwell, Monica Allen, Jeffery Allen and Gennady Shvets\*

# Electrically defined topological interface states of graphene surface plasmons based on a gate-tunable quantum Bragg grating

<https://doi.org/10.1515/nanoph-2019-0108>

Received April 8, 2019; revised June 14, 2019; accepted June 16, 2019

**Abstract:** A periodic metagate is designed on top of a boron nitride-graphene heterostructure to modulate the local carrier density distribution on the monolayer graphene. This causes the bandgaps of graphene surface plasmon polaritons to emerge because of either the interaction between the plasmon modes, which are mediated by the varying local carrier densities, or their interaction with the metal gates. Using the example of a double-gate graphene device, we discuss the tunable band properties of graphene plasmons due to the competition between these two mechanisms. Because of this, a bandgap inversion, which results in a Zak phase switching, can be realized through electrostatic gating. Here we also show that an anisotropic plasmonic topological edge state exists at the

interface between two graphene gratings of different Zak phases. While the orientation of the dipole moments can differentiate the band topologies of each graphene grating, the angle of radiation remains a tunable property. This may serve as a stepping stone toward active control of the band structures of surface plasmons for potential applications in optical communication, wave steering, or sensing.

**Keywords:** graphene plasmons; band topology; active metasurface; topological interface state.

## 1 Introduction

*Motivation.* Topological photonics is a new and exciting area of optical science that deals with and employs the robust characteristics of periodic structures, also known as topological indices, to produce scattering-free, localized optical excitations. Such excitations exist at the edges or domain walls of photonic topological insulators (PTIs) [1] and are spectrally located inside PTIs' bandgaps. The PTI concept is intimately connected to that of the topological insulator [2, 3], which is one of the most vibrant areas in today's condensed matter physics. While most emphasis in topological photonics has been on two- and three-dimensional PTIs supporting either edge or surface states [1, 4–14], it is well known that even one-dimensional photonic crystals (PhCs) can have topological properties. As was the case with 2D and 3D PTIs, the original concept for such confined zero-dimensional states emerged from studying electronic systems such as polyacetylene [15]. The Su-Shrieffer-Heeger (SSH) model, which was developed to explain “soliton” formation in 1D long-chain polyenes, was crucial in interpreting the experimentally discovered interface states, which require less energy to excite than the gap energy and play a fundamental role in the charge-transfer doping mechanism.

\*Corresponding authors: Zhiyuan Fan, PhD and Dr. Gennady Shvets, School of Applied and Engineering Physics, Cornell University, Ithaca, NY 14853, USA, e-mail: zf86@cornell.edu (Z. Fan); gs656@cornell.edu (G. Shvets). <https://orcid.org/0000-0002-9312-2271> (Z. Fan)

**Shourya Dutta-Gupta:** Department of Materials Science and Metallurgical Engineering, Indian Institute of Technology Hyderabad, Sangareddy, Telangana 502285, India

**Ran Gladstone and Maxim Shcherbakov:** School of Applied and Engineering Physics, Cornell University, Ithaca, NY 14853, USA

**Simeon Trendafilov, Monica Allen and Jeffery Allen:** Air Force Research Laboratory, Munitions Directorate, Eglin AFB, FL 32542, USA

**Melissa Bosch and Minwoo Jung:** School of Applied and Engineering Physics, Cornell University, Ithaca, NY 14853, USA; and Department of Physics, Cornell University, Ithaca, NY 14853, USA

**Ganjigunte R. Swathi Iyer:** ASEE/NRL Postdoctoral Fellow, Residing at NRL, Washington, DC 20375, USA

**Alexander J. Giles and Boris Feigelson:** U.S. Naval Research Laboratory, Washington, DC, USA

**Joshua D. Caldwell:** Department of Mechanical Engineering, Vanderbilt University, Nashville, TN 37212, USA

More recently, a variety of periodic platforms trying to emulate the SSH model have been proposed, and robust zero-dimensional states have been found in acoustic crystals [16–18], PhCs [19–23], and even cold atoms in optical lattices [24, 25]. Our emphasis is on the photonic systems in the remainder of this article. In such 1D PhCs, topological properties of Bloch bands can be characterized by a topological invariant, referred to as the Zak phase. It is a geometric phase resulting from completing the loop of adiabatic evolution of the relevant bulk wavefunction (e.g. a scalar electric potential field on graphene of a plasmon mode in the electrostatic approximation) across the Brillouin zone [26]. A nontrivial Zak phase predicts the existence of protected SSH interface states localized at the boundaries of the 1D PhCs [27–29]. Such boundaries also include the domain walls between two PhCs sharing the same photonic bandgap but characterized by different Zak phases.

In recent studies, the flip of the Zak phase was found to be related to the inversion of Bloch bands [26]. Moreover, it was found to be connected to experimentally measurable surface impedance or reflection coefficients from the PhC interface [20, 27], thereby establishing a connection between physical observables and the Zak phase. However, because, by their very definition, PhCs enable the creation of bandgaps due to Bragg scattering, both the lattice period and the confinement length of the interface states must be comparable to the wavelength of light for conventional photonic structures constructed out of metals and dielectrics. For example, it is challenging to construct a conventionally composed PhC operating in the mid-infrared (MIR) portion of the spectrum that confines light to smaller than a micrometer.

Moreover, a predesigned dielectric- or metal-based PhC cannot be easily changed in time. Therefore, active control of the SSH interface states in conventional PhCs is challenging. In this work, we demonstrate how a special class of electromagnetic excitation – graphene surface plasmon polaritons (GSPPs) – can be utilized to produce strongly localized (sub-wavelength) interface states at the domain wall between two metallic electrically biased 1D Bragg gratings described below. The 1D metallic gratings affect the propagation of GSPPs in two distinct ways. First, they directly interact with the graphene plasmons by producing strong horizontal and vertical dipole moments. Second, when an electric field is applied between graphene and the grating, the carrier density in graphene is also modulated. The resulting modulation of the chemical potential modulates graphene's conductivity, thereby inducing additional Bragg scattering of GSPPs. Thus, the metallic grating simultaneously serves as a metagate and

a PhC. The interplay between these two scattering pathways can either open or close a propagation bandgap for GSPPs at the center or edge of the Brillouin zone. We demonstrate that the Zak phases of the two interface-forming 1D graphene-plasmonic Bragg gratings can be controlled through electrostatic gating, thereby controlling the properties of the interface states. As we demonstrate in the following text, such interface states can be excited in the far-field. The conceptual device to be presented in this study has three distinct new features compared to a previous proposal [14]. In the current 1D-periodic metasurface, the band topology and the Zak phase can be controlled with fast, real-time electrostatic gating. Secondly, these 1D gratings are electrically disconnected from each other. It allows electromagnetic waves to directly access surface plasmon polaritons. Far-field techniques can be applied to interrogate the band topologies of plasmons. Last but not least, a domain wall separating two topologically distinct crystals is now reconfigurable because the metagates are individually tunable.

*Brief description of graphene surface plasmon polaritons.* Since its first production by exfoliation from graphite [30–32], monolayer graphene has attracted a tremendous amount of research interest. In particular, graphene-based metasurfaces have been developed into a technologically important platform for the testing of innovative ideas and applications [33–61]. One major advantage of graphene is that it supports plasmons that can operate over the terahertz (THz) to mid-infrared (mid-IR) spectral range, where many important applications are implemented. As compared with the metallic counterparts, GSPPs are much more confined and significantly less lossy, leading to the design of smaller footprint devices featuring higher field enhancements and longer propagation lengths [34, 44, 62–66]. In addition, its infrared (IR) properties can be actively modified and modulated [65, 67, 68], owing to the pronounced ambipolar electric field effect [69, 70].

One of the most remarkable and attractive properties of graphene is that the Fermi level of the free carriers (i.e. its chemical potential) can be continuously tuned from its valence band to the conduction band by the injection of charge carriers, providing linear control of the frequency-dependent optical conductivity of graphene over a very wide spectral band. Molecular doping [71] and electrostatic gating [72] are two parallel approaches to achieve this goal. In particular, the electrostatic gating of graphene using patterned metasurfaces benefits from semiconductor-compatible fabrication technologies and thus has been widely implemented in both fundamental and advanced device research. Using such approaches, the conductivity of graphene can be changed by at least

two orders of magnitude [31, 73]. The control of local Fermi levels and conductivity of graphene in practice can be utilized to modulate optical transmission [36–39, 60, 61] through graphene-based metasurfaces, which is useful for sensing or optical communications applications for instance. It can also create p-n junctions or quantum dots confined spatially within the graphene layer by more sophisticated patterning of local carrier distribution, which allows for the manipulation of electrons [74–77].

Patterning of graphene with permanently imprinted geometries has been previously proposed [60, 61, 78, 79]. On the other hand, multiple possibilities of transforming a uniform carrier density distribution within a graphene sheet into a complicated spatial dependence, e.g. into a periodic Bragg grating, have also been demonstrated [41, 80–84]. The one approach that does not require graphene patterning of chemical doping relies on the electrostatic field being periodically shaped using a patterned metasurface or grooved substrates [14, 85]. Potential applications in active plasmonics could also benefit from the ultrafast process of carrier generation and relaxation in graphene, as the Fermi level has been demonstrated to be electrostatically adjusted at sub-nanosecond time scales [86]. Marrying the sub-wavelength nature of graphene plasmonics with local nanoscale patterning of the carrier density distribution in graphene-based metasurfaces thus offers promising opportunities in active and ultrafast manipulation of light at the nanoscale.

The rest of this article is organized as follows. In Section 2 we discuss the physics of controlling the carrier density in graphene using a periodic metallic metagate. Quantum capacitance is taken into account by requiring the constancy of the electrochemical potential in graphene. In Section 3, we briefly introduce the calculation of the Zak phase for Bloch plasmon bands that emerge as a result of the periodic modulation of carrier density. The photonic band structure of GSPPs in a periodic chemical potential of graphene is calculated, and the concepts of band inversion and bandgap closing are introduced. In Section 4, we show numerical simulation of far-field transmission spectra of a graphene device applied with different gate voltages. The manifestations of band inversion and bandgap closing in reflection/transmission spectra strongly rely on the presence of metallic top gates. Localized interface states at the interface between graphene-based gratings of different Zak phases are identified, and their coupling to the incident far-field radiation is calculated as a proof of concept. We show that an interface state can be anisotropic because of the hybridization of wavefunctions from the adjacent 1D PhCs with different Zak phases. In addition, because the hybridization strongly

depends on the localization of the evanescent mode into the interface-forming PhCs, the effective polarizability tensor of the interface state becomes tunable, making it a promising fundamental building block for actively tunable electro-optic devices. Finally, quantum nonlocality effects are discussed in Section 5. We compare the tunability of the band structures calculated using both COMSOL Multiphysics with a local Drude conductivity and a program developed in house by Jung et al. [14]. The latter takes into account nonlocal effects [67].

## 2 Periodically gated graphene

### 2.1 Graphene conductivity

Properties of GSPPs interacting with light rely on the response of oscillating carriers of graphene. Such response can be described by an optical conductivity, which was previously derived from a linear response of electronic current to external fields for a tight-binding Hamiltonian of carbon atoms sitting on the honeycomb lattice [87]. It was found that graphene with a uniform distribution of carriers has the following response in the infrared regime:

$$\sigma_g \equiv \frac{e^2}{4\hbar} \left[ \frac{1}{2} + \frac{1}{\pi} \tan^{-1} \frac{\hbar\omega - 2E_F}{2k_B T} - \frac{i}{2\pi} \ln \frac{(\hbar\omega + 2E_F)^2}{(\hbar\omega - 2E_F)^2 + (2k_B T)^2} \right] + \frac{e^2}{4\hbar} \left[ \frac{8ik_B T}{\pi\hbar(\omega + i\tau^{-1})} \ln 2 \cosh \frac{E_F}{2k_B T} \right], \quad (1)$$

where  $\sigma_g$  is the surface conductivity depending on the temperature  $T$ , frequency  $\omega$ , local chemical potential  $E_F$ , and scattering time  $\tau$  due to carrier scattering [88]. We will take the low-temperature and low-photon-energy limit for our application. Therefore, it leads to a Drude model after those considerations:

$$\sigma_g = \frac{ie^2 E_F}{\pi\hbar^2} \frac{1}{\omega + i\tau^{-1}}. \quad (2)$$

We use Eq. (2) in both the quasi-electrostatic model and full-wave simulation of the optical properties of GSPPs. The chemical potential  $E_F$  should be taken as a constant if the carrier distribution is uniform. But, here, the surface conductivity of graphene is further assumed to be a local property of the carrier density distribution. We extend the relationship of local chemical potential to be position-dependent,  $E_F(x) = \hbar v_F \sqrt{\pi n(x)}$ . This allows us to conveniently prescribe a Fourier series of  $E_F(x)$  and  $\sigma_g(x)$

in a periodic system for numerical simulations, with coefficients of both expansions connected through Eq. (2). A periodic carrier distribution can be induced by gating the graphene periodically using a metallic metasurface. This will be discussed in the next section utilizing an intuitive electrostatic model. However, such a conductivity model solved from electrostatics needs to be modified in the presence of nonlocal effects when a finite wavevector of GSSP is considered. This nonlocal effect will also be evaluated for our application at the end of this study.

## 2.2 Description of the graphene-based photonic platform

In Figure 1A, we show a schematic of the photonic platform to be analyzed in this work. It is a double-gated device, with a single-layer graphene (SLG) encapsulated between two hexagonal boron nitride (hBN) layers, and a periodic metagate placed atop of the structure. The hBN layers provide protection of the SLG from the environment and ensure that the electronic transport properties correspond to the intrinsic values of graphene. A periodically patterned metal metasurface serves as the top gate with an electric potential  $V_1$ , thus controlling the carrier density  $n(x)$  inside the SLG with high spatial precision. From a practical perspective, the geometric dimensions of graphene-based devices, such as the metasurface periodicity  $P_x$ , can potentially be made at deeply sub-wavelength length scales for the MIR GSSPs:  $2\pi/P_x \sim 2\pi/\lambda_0 \cdot n_{\text{eff}}$ , when MIR GSSP with extremely high effective index

$n_{\text{eff}} > 100$  is excited [67]. Such nanoscale patterning of chemical potential inside the SLG can be accomplished using e-beam lithographically defined metallic metagates. Both the amplitude of modulation and sharpness of  $n(x)$  and of the corresponding chemical potential  $E_F(x)$  are absolutely crucial for the control of the photonic bandgap. One additional degree of control over optical properties of the SLG comes from the back gate kept at the potential  $V_2$ . The back gate serves the role of contributing to an offset in the average carrier density  $n_0 = \langle n(x) \rangle$  in the SLG and, therefore, will be used to adjust the mid-gap frequency.

Unlike a perfect electric conductor (PEC), which completely screens the tangential component of the electric field, graphene does not do so, especially at low bias of electrostatic gating. Therefore, while the electric potential  $\varphi$  is a constant at the surface of a PEC, the quantity that remains constant on the surface of graphene is the so-called electrochemical potential. The underlying physics is governed by [89]

$$e\varphi + E_F = eV_g, \quad (3)$$

where the energy needed for supplying one extra electron into graphene is described by an electrochemical potential energy  $eV_g$ , which should be equal to the increase in potential  $e\varphi$  and an extra  $E_F$  needed to inject the electron into graphene. In a general case, voltages are applied to the top and bottom gates, while a constant electrochemical potential can be assumed in the graphene, as shown in Figure 1A. A solution is found by implementing the nonlinear boundary condition of Eq. (3) in a finite element (FEM) solver [90]. For the specific design (Figure 1A), we

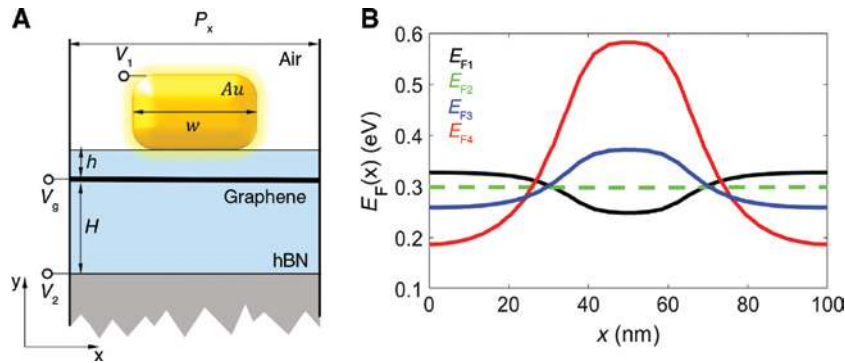


**Figure 1:** An electrostatic model of patterning chemical potential on a double-gated graphene encapsulated by two hBN layers.

(A) A side view of the unit cell of graphene metasurface. Periodic gold metagates are supplied with top gating voltage  $V_1$ , graphene has  $V_g = 0$  as electrochemical potential, and a back gate is far away from the graphene which has  $V_2$  as the back gate voltage. The back gate can be a monolayer of graphene or doped silicon substrate. (B) Using the geometry in (A), local carrier density distribution is calculated and it defines  $E_F(x)$ , which is the local Fermi level of free carriers. In this example,  $h = 6$  nm,  $H = 50$  nm,  $w = 40$  nm, and  $P_x = 100$  nm. The height of Au bars is 30 nm, but the thickness plays a less significant role in either electrostatic gating or infrared scattering. Electrostatic permittivity of hBN is  $\epsilon_{xx} = 7$  and  $\epsilon_{yy} = 4.5$ . Gating voltages are  $V_1 = -0.35$  V and  $V_2 = 11$  V for the black curve,  $V_1 = 0.29$  V and  $V_2 = 9.0$  V for the green dashed curve,  $V_1 = 1.3$  V and  $V_2 = 6.3$  V for the blue curve, and  $V_1 = 4.5$  V and  $V_2 = 1.7$  V for the red curve.

**Table 1:** Fourier expansion coefficients of  $E_F$  functions in Figure 1B.

(eV)	$E_F^{(0)}$	$E_F^{(1)}$	$E_F^{(2)}$
$E_{F1}$	0.300	0.041	-0.011
$E_{F2}$	0.298	0.000	-0.002
$E_{F3}$	0.301	-0.058	0.020
$E_{F4}$	0.347	-0.206	0.048

calculated the local  $E_F$  functions for various combinations of input gating voltages, as shown in Figure 1B. For a periodic structure, we can expand the local  $E_F$  functions as a Fourier series

$$E_F(x) = E_F^{(0)} + E_F^{(1)} \cos Gx + E_F^{(2)} \cos 2Gx + \dots, \quad (4)$$

where  $G = 2\pi/P_x$ , and  $P_x$  is the period of the grating. This expansion can also be applied to the  $E_F$  functions in Figure 1B. We give the expansion coefficients in Table 1. These profiles can change the photonic band structures of GSPPs, and they will be used as local conductivity input for optical simulations in the following sections. Note that the green dashed  $E_F$  profile in Figure 1B is flat, corresponding to a uniform distribution of carrier density. As expected from Eq. (3), its electric potential equals the top gate bias, instead of the 0 electrochemical potential supplied on graphene. This means no carriers are effectively contributed by the top gate.

For now, we focus on the effect of the geometric parameters of graphene-based metasurfaces, such as the metagate-to-SLG spacing  $h$  and the grating periodicity  $P_x$  (see Figure 1A for the definitions of the geometric parameters), and on the spatial Fourier components of the periodic  $E_F(x)$ . We consider a simple parallel capacitor model. The model is applied to the SLG and to the bottom surface of the metagate. The two are separated by the distance  $h$ . Graphene is assumed to be electrochemically grounded, i.e.  $V_g = 0$ . To induce spatial modulation of carrier density in graphene, we assume that a spatially harmonic potential  $V(x)$  is applied to the top plate:

$$V = V_0 + \delta V \sin kx, \quad (5)$$

where  $V_0$  is a constant,  $\delta V$  characterizes a perturbation, and  $k$  is the spatial frequency of the Fourier component. The carrier density of graphene can be found in the following form in the small modulation limit:

$$n(x) \approx \frac{\varepsilon_0 V_0}{e h} \left( 1 + 2kh \frac{\delta V}{V_0} \frac{e^{kh}}{\left(1 + \frac{\alpha k}{2\sqrt{a}}\right) e^{2kh} - \left(1 - \frac{\alpha k}{2\sqrt{a}}\right)} \sin kx \right), \quad (6)$$

where  $\alpha = \sqrt{4\pi\varepsilon_0} / e \cdot \hbar v_F / 2e$  is a parameter that depends on the properties of the graphene layer and on the spatial scale of the imposed voltage perturbation, and  $a = V_0/h$  is the average gate field applied between the SLG and the gate. The term with a nonvanishing  $\alpha$  accounts for an unscreened electric field behind the graphene sheet as compared to the response of a perfect metal. We note that the combination  $E_{gr} \equiv \alpha^2 k^2 = (v_F/c)^2 (2er_e)^{-1} (\hbar^2 k^2 / 2m)$  has the dimension of the electric field inside graphene. Here,  $r_e = e^2/mc^2$  is the classical electron radius, and  $v_F/c \sim 1/300$ . For example, for  $k = 2N\pi/100$  nm, we estimate that  $E_{gr} \sim N^2 10^{-4}$  V/nm. The relative magnitude of  $E_{gr}$  and the imposed gate field  $V_0/h$  determines the degree of screening of the imposed spatially varying electrostatic potential by graphene compared to a PEC. For example, if  $E_{gr} \ll V_0/h$ , then graphene behaves as a PEC. Note that Eq. (6) has used the assumption that  $\delta V/V_0 \ll 1$ ; therefore the scaling law of  $E_{gr}$  is only used to emphasize the significant contribution to screening effects from high-order spatial harmonics in the carrier density distribution.

Equation (6) also indicates that the carrier density profile becomes flattened as  $kh$  increases. For a metagate that is over 100 nm away from the graphene, this will result in a vanishing variation in the charge carrier density set by the varying potential, which is characterized by  $\delta V/V_0 < 0.5$ . The value of  $\delta V/V_0$  in principle can be estimated from an FEM simulation, depending on the geometry and input voltages to be used. For a metagate that is less than 10 nm removed from the graphene layer, the Fourier transform of the resultant  $E_F(x)$  can have considerable presence of the high-harmonic Fourier components. These harmonics are essential for creating propagation bandgaps for the GSPPs.

### 3 Optical properties of GSPPs

#### 3.1 Calculation of the photonic band structure of GSPPs supported by graphene with nonuniform chemical potential

In order to demonstrate clearly the physics of band inversion due to a spatially varying surface charge distribution, we first analytically calculate the band structures of graphene plasmon modes in a much simpler scenario, that is, a graphene sheet suspended in air. This is done to avoid the complications related to optical phonon excitations in the hBN encapsulation layers [55, 56, 91] and to the interaction

of the GSPPs with a metallic metasurface. Surface plasmon on graphene is deeply sub-wavelength, and its electrodynamic formalism can be approximated using electrostatics. For a free-standing graphene layer in air, electric field of a resonant GSPP mode can be found by solving the Poisson equation for a potential field with properly imposed boundary conditions across the graphene. The basis of a solution in free space takes the following form:

$$\phi_{m,k}^{\pm}(x,y) = e^{ikx} e^{imGx} e^{\pm\alpha_{m,k}y}, \quad (7)$$

where  $k$  is the Bloch wave number,  $G = 2\pi/P_x$  is the lattice vector due to a periodic modulation of carrier distribution,  $m$  is an order index used in Fourier expansion, and  $\alpha_{m,k} = |k + mG|$  is the transverse decay constant in the electrostatic limit for the  $m$ th evanescent wave. The symbol  $\pm$  denotes whether the potential field is above or below the graphene sheet. A GSPP mode has a trial potential field, which can be expanded on such basis [Eq. (7)]:

$$\varphi_k^{\pm}(x,y) = \sum_m c_{m,k}^{\pm} \phi_{m,k}^{\pm}(x,y) = e^{ikx} u_k(x,y), \quad (8)$$

with expansion coefficients  $c_{m,k}^{\pm}$  of a particular GSPP mode to be determined by matching boundary conditions.  $u_k(x,y)$  is the periodic part of the wavefunction and will be used for the evaluation of the geometric Zak phase. The oscillating charges must satisfy the following three conditions:

$$\partial_x \varphi_k^+ |_{y=0} = \partial_x \varphi_k^- |_{y=0}, \quad (9)$$

$$-\partial_y \varphi_k^+ |_{y=0} + \partial_y \varphi_k^- |_{y=0} = \sigma_s / \epsilon_0, \quad (10)$$

$$i\omega\sigma_s + \partial_x (\sigma_g \partial_x \varphi_k |_{y=0}) = 0, \quad (11)$$

where  $\sigma_s$  is the surface charge density, and  $\sigma_g(x) = \sum_m \sigma_g^{(m)} e^{imGx}$  is the Fourier expansion of the local conductivity of graphene. These three equations denote, respectively, the continuity of the transverse electric field, Gauss's law of surface charges, and the continuity equation of oscillating carriers.

Using the trial solution Eq. (8) with unknown coefficients and Eqs. (9)–(11), we can derive the following eigen equation [Eq. (12)] and solve it for the eigen modes and eigen frequency in the momentum space, given either artificial or realistic chemical potential distributions using the Fourier expansion

$$\beta \sum_{m'} 2E_F^{(m-m')} \frac{(\tilde{k} + m')(\tilde{k} + m)}{\tilde{\alpha}_{m',k}} c_{m',k} = (\hbar\omega)^2 c_{m,k}, \quad (12)$$

where  $\beta = \frac{e^2}{4\pi\epsilon_0} G$  and  $E_F^{(m-m')} = -i\hbar^2 \omega \sigma_g^{(m-m')} / e^2$ , after the scattering time constant  $\tau$  from the conductivity equation

[Eq. (2)] is neglected for this theoretical analysis.  $\tilde{k}$  and  $\tilde{\alpha}_{m,k}$  are the Bloch number and transverse decay constant normalized to magnitude of the lattice vector. In the first example to demonstrate bandgap inversion, we solved for the eigen frequencies for four different carrier distributions as those indicated in the captions of Figure 2. The prescribed (e.g. induced by chemical doping) profile of the chemical potential is assumed to be of the form of Eq. (4).

This spatial dependence is sufficient for opening the first bandgap at the  $\Gamma$ -point with a nonzero  $E_F^{(2)}$  coefficient. For generality, a nonvanishing  $E_F^{(1)}$  is also assumed. A band inversion at the  $\Gamma$ -point can be observed by comparing Figure 2A and B, or Figure 2A and C, when the  $E_F^{(2)}$  parameter is tuned across zero. We can also see that the symmetry property of the modes change as a result.

### 3.2 Band topology in 1D graphene metasurfaces

Band inversions are associated with a change of band topology, and are characterized by a 1D geometric phase called the Zak phase. The Zak phase is a robust index that characterizes the 1D topological properties of bulk bands. It is defined as

$$\theta_n^{\text{Zak}} = i \int dk \langle u_{n,k}^* | \partial_k | u_{n,k} \rangle, \quad (13)$$

where the integration of  $k$  is performed inside the first Brillouin zone for any band  $n$  using its Bloch wavefunctions  $u_{n,k}(x)$  [26]. Another way to calculate the Zak phase is to use its discretized form as was previously utilized in [16]:

$$\theta_n^{\text{Zak}} = -\text{Im} \sum_{\{k_i\}_{i=1}^N} \ln \int_{\text{cell}} dx u_{n,k_i}(x)^* u_{n,k_{i+1}}(x), \quad (14)$$

where  $k_1, k_2, \dots, k_N$  are taken as a sequential wave number partition of the Brillouin zone, with  $k_1 = k_N$  to close the loop. Its numerical evaluation is straightforward when the Bloch wavefunctions for each band  $u_{n,k}(x)$  are known from solving Eq. (12), or more generally from FEM eigen frequency simulations.

Although it is stated that the topological property of a bandgap is determined by the summation of the Zak phases [Eq. (14)] of all the bands below this gap, it is however relevant to know the symmetry of the two modes at the bandgap of interest in this 1D case, given that the Zak phase can be uniquely associated with the symmetries of modes at the center and edge of each band [16, 20]. Flipping the symmetry at any lower bandgap will lead to a  $2\pi$  total Zak phase change, while flipping the symmetry

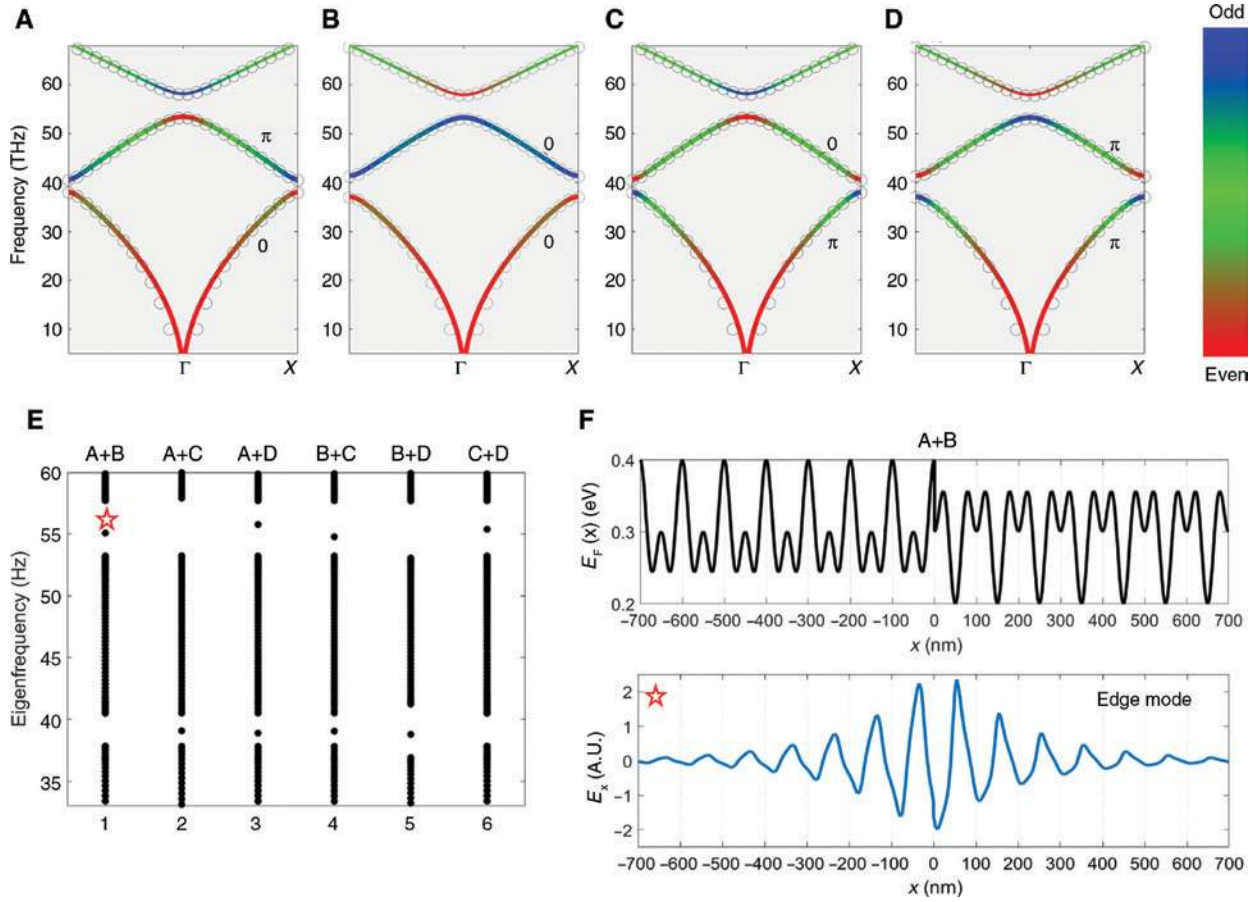


**Figure 2:** A simplified model platform for investigating topological properties of 1D graphene metasurface: a suspended nonuniformly gated graphene layer with the chemical potential given by Eq. (4).

Four different combinations of  $(E_F^{(1)}, E_F^{(2)})$  are used to create band gaps at the  $\Gamma$ - and  $X$ -points. (A)  $E_F^{(1)} = 0.05$  eV,  $E_F^{(2)} = 0.05$  eV,

(B)  $E_F^{(1)} = 0.05$  eV,  $E_F^{(2)} = -0.05$  eV, (C)  $E_F^{(1)} = -0.05$  eV,  $E_F^{(2)} = 0.05$  eV, and (D)  $E_F^{(1)} = -0.05$  eV,  $E_F^{(2)} = -0.05$  eV. The circles are solved by COMSOL

Multiphysics and the colored solid lines are obtained by solving Eq. (12). Each band is color-coded according to the symmetries of full wavefunctions. The Zak phases are numerically calculated. (E) Eigen modes of bridged graphene Bragg gratings are simulated for all different combinations of those from (A)–(D). Interface states present in various bandgaps when the two graphene Bragg gratings different in Zak phase. (F) For the case labeled with a red hollow star, local chemical potential distribution and a localized profile of an interface state are plotted.

of modes at the bandgap of interest leads to a  $\pi$  total Zak phase change. In Figure 2, we numerically demonstrate for the second band that the Zak phase is correlated with the mode symmetries. Correspondingly, the symmetry of the wavefunctions is color-coded, and the single-band Zak phases are labeled.

To approximate the Hamiltonian in Eq. (12), we take into consideration only the three lowest Bloch bands, namely the  $m=0$  and  $\pm 1$  bands. Our model Hamiltonian is recast into two parts in Eq. (15). The first term has plane wave solutions of uniformly gated graphene and two perturbed terms describing the spatial modulation up to the second order of the  $E_F$  expansion, which is minimally required to couple the  $m=\pm 1$  bands:

$$H_k = E_F^{(0)} \begin{pmatrix} 1-k & 0 & 0 \\ 0 & |k| & 0 \\ 0 & 0 & 1+k \end{pmatrix} + E_F^{(1)} \begin{pmatrix} 0 & -k & 0 \\ \frac{k}{|k|}(k-1) & 0 & \frac{k}{|k|}(k+1) \\ 0 & k & 0 \end{pmatrix} + E_F^{(2)} \begin{pmatrix} 0 & 0 & -(k+1) \\ 0 & 0 & 0 \\ k-1 & 0 & 0 \end{pmatrix}. \quad (15)$$

This model Hamiltonian can be easily solved, and quantitative comparison are made with the band structures plotted in Figure 2A–D.

### 3.3 Interface state

One important application of the Zak phase is that it establishes the relation of the existence of an interface state through the comparative difference in the Zak phase between bulk materials on either side of this edge state. Simulations show that the phase of a reflected beam from a bulk crystal in the bandgap can have a phase difference of  $\pi$  when the bulk Zak phase is different by the same quantity, which has also been demonstrated using PhCs [16]. Both simulations and experiments have probed the phase relations between the different electromagnetic field components of an evanescent wave decaying into the bulk crystal. It suggests that an edge state can exist in the bandgap common to both adjacent bulk crystals when the total Zak phase of the bandgaps is different by  $\pi$ . On our graphene platform, we verify this conclusion using the four graphene Bragg gratings in previous simulations, in which all bandgaps have been labeled a Zak phase. We show the frequency of eigen modes of all six combinations of bridged Bragg gratings (Figure 2E, F). Simulations were performed on a 100-unit cell-long graphene grating with a Floquet periodicity. Divided in the middle, each 50 unit cells are given a carrier density chosen from the four configurations. Figure 2E shows consistent results of the presence of interface states as predicted by the Zak phase analysis.

## 4 Far-field manifestation

In a practical design, the GSPP modes have an evanescent field profile in the vertical direction, which inevitably interacts with the off-resonance spoof plasmon modes [92] supported by the metagates in the vicinity. Thanks to material dispersion of the highly anisotropic hBN [91, 93], the vertical decay of infrared plasmons is faster than that of the gating electrostatic field. Therefore, it is possible to offset the GSPP-spoof-plasmon interaction by tuning the top gate voltage in an intuitively perturbative model, with the bandgap inversion occurring when the voltage on the top gate is nonzero. We chose the demonstration operational frequency to be near 28 THz [91]. The closing of a bandgap can be manifested as a merging of a pair of transmission dips in the spectra of oblique transmission through the structure, considering that the metasurface unit cell is extremely sub-wavelength. In addition, this graphene Bragg grating can be used to create a resonating interface state by setting the various top metagates to two slightly different sets of applied biases and forming a domain wall in the middle of the graphene Bragg grating [94].

### 4.1 GSSP band inversion

To observe band inversion in 1D graphene-based metasurfaces using far-field illumination, we simulated transmission properties (Figure 3) of the device with an extra substrate consisting of a 200-nm-thick SiO<sub>2</sub> layer and silicon. We clearly see two transmission dips in the spectra for  $E_{F_1}(x)$  (black line) and  $E_{F_4}(x)$  (red line) profiles. Because of the deeply sub-wavelength unit cell size of the metagate, the spectral positions of the transmission dips only slightly shift their frequency as the incident angle varies from  $\theta=20^\circ$  to  $\theta=70^\circ$ . Profiling the excited near-fields of the metasurface at the dip locations reveals two important effects. First, we observe that the deeper transmission dips (especially at small incidence angles) are associated with the excitation of the  $E_x$ -even modes. This is because the even modes have a stronger electric dipole moment  $p_x$  and can be excited by a p-polarized light even under small-angle oblique incidence. Second, we observe that band inversion indeed occurs when the chemical potential profile switches from  $E_{F_1}(x)$  to  $E_{F_4}(x)$  cases. This is particularly clear for the small-angle ( $\theta=20^\circ$ ) transmission spectra, where the transmission dip at the even mode clearly jumps from low to high frequencies as the gating voltages change from Case 1 (corresponding to the  $E_{F_1}(x)$  profile) to Case 4 (corresponding to the  $E_{F_4}(x)$  profile). For large incidence angles ( $\theta=70^\circ$ ), both the high- and low-frequency dips are observed in the spectra.

Considerable departure from Cases 1 and 4 can be observed in the spectra corresponding to the Case 3 ( $E_{F_3}(x)$  chemical potential profile). Almost no transmission dips are observed for small incidence angles, and only a single (merged) dip is observed for the largest incidence angles. This suggests that the two modes of opposite symmetry (even and odd) cross each other at the  $\Gamma$ -point for the gating voltages. In other words, the bandgap closes for the specific combination of the chemical potential profile  $E_{F_3}(x)$  and the metal grating location. The physical interpretation of this result is as follows. As GSPPs propagate along the 1D graphene metasurface, they experience backscattering due to the two channels produced by two distinct Bragg gratings: (i) the metallic grating located in close proximity of the SLG, and (ii) the variable-conductivity grating defined by the  $E_r(x)$  profile. The two scattering channels can interfere in a constructive or destructive way. The interference become destructive and there is an exact cancellation between the two scattering channel in Case 3. Therefore, the bandgap closes because a forward-traveling GSPP no longer scatters into its backward-traveling counterpart. On the other hand, channel (ii) overcomes channel (i) in Case 4 because of the large variation of  $E_{F_4}(x)$  inside the unit cell (compare the red

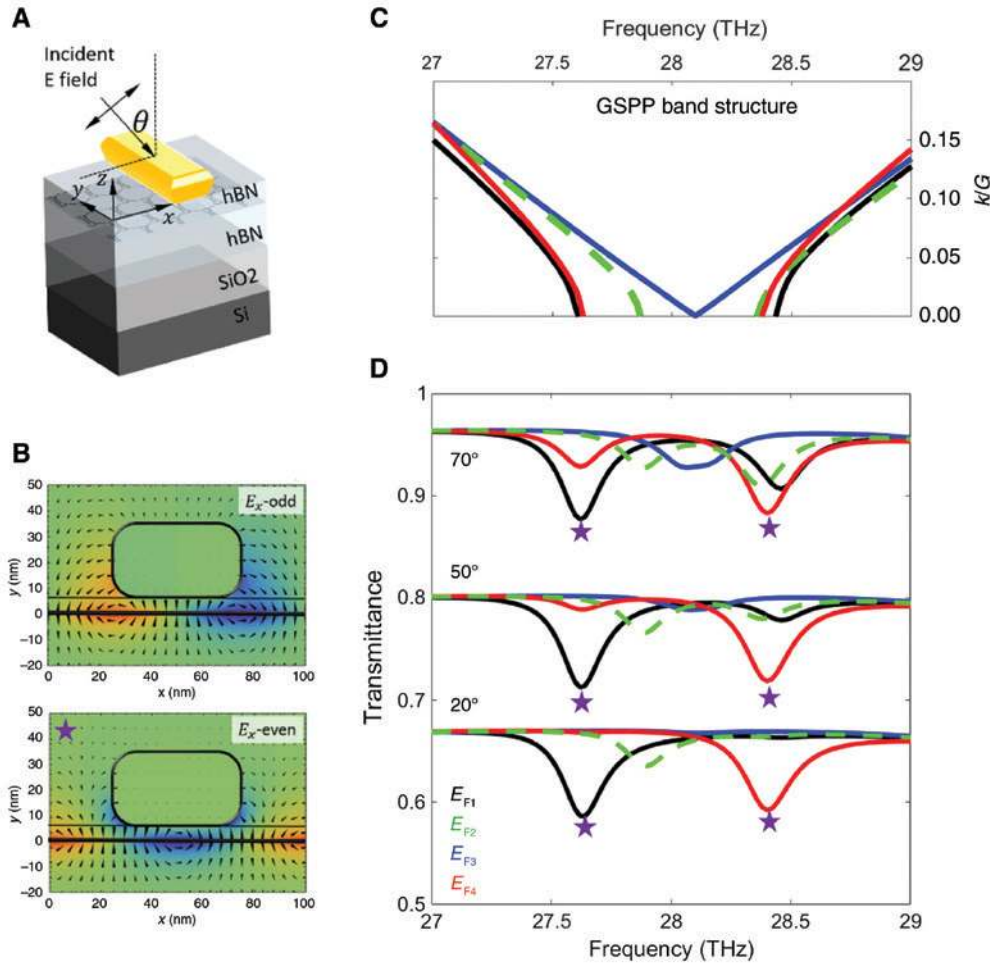


**Figure 3:** Farfield interrogation of GSP band inversion.

(A) Illustration of the mounting of incident field and a unit cell of the structure. Here, silicon and 200-nm silicon dioxide are used as the substrates. We may assume that a uniform monolayer graphene can be deployed between  $\text{SiO}_2$  and the bottom layer hBN as the back gate, but it can be neglected in mid-IR transmission simulations. (B) Typical field profiles of  $E_x$ -odd and  $E_x$ -even modes whose optical responses are observed as transmission dips. Under normal or small-angle incidence, the modes at pronounced dips have stronger transverse dipole moments therefore are labeled as the even modes by a purple star. Respectively, the colored (C) band dispersion near the  $\Gamma$ -point and (D) transmission spectra correspond to the local carrier density distribution calculated in Figure 1B for various incident angles. In these simulations, the conductivity equation [Eq. (2)] is used, and scattering time of carriers is chosen to be 500 fs.

line Figure 1B to other lines in the same figure). However, the frequency order of the modes in Case 4 is now opposite to that in Case 1. As we have shown previously, this is connected to the sign change of the second Fourier harmonic of the chemical potential  $E_F(x)$  between Cases 1 and 4.

Case 2 (green dashed curve corresponding to  $E_{F2}(x)$  profile) presents an interesting case when the surface conductivity is flat while only the scattering channel (i) is on. This allows us to observe GSP scattering only due to metal metagates. When GSP interacts with a uniform metal gate that is placed at  $h$  over the graphene, it is known that the GSP forms an acoustic mode for small  $h$  [95]. We use the electrostatic approximation discussed above and show that its mode dispersion is as follows:

$$k(1 - e^{-2\sqrt{\epsilon_{xx}/\epsilon_{yy}}kh}) = \frac{2\pi\hbar^2\sqrt{\epsilon_{xx}\epsilon_{yy}}}{e^2E_F}\omega^2, \quad (16)$$

where  $E_F$  is the constant chemical potential, and  $\epsilon_{xx}$  and  $\epsilon_{yy}$  are, respectively, the dielectric tensor elements of the surrounding anisotropic material along the graphene sheet and perpendicular to it.  $k$  is the wave number for GSP modes. For small  $h$ , GSP frequency is linear in wave number and it is significantly red-shifted as compared with a GSP on a free-standing graphene sheet. This offers an intuitive picture of the mode frequency shift due to a flat metal gate. However, when metagates are periodically patterned, it supports evanescent modes in the air gap as well

as a TEM mode that channels plasmon mode energy into the far-field. Propagating acoustic modes would couple under these scattering processes and form a bandgap as shown in Figure 3C and D (green dashed curves). Its  $E_x$ -even mode should take the lower frequency because a metal strip is sitting atop of its mode anti-node, offering more red shift of its resonance frequency than the  $E_x$ -odd mode. This also helps us to identify the  $E_x$ -even modes for any other band structure of the same topological phase before bandgap closing, in addition to the pronounced far-field signature.

## 4.2 Anisotropic interface state

It is known that leaky photonic modes can be utilized to probe and visualize topological states via Fano resonances [96]. The nonvanishing dipole moments carried by the topological edge state come from an intrinsic property of at least one of the bulk modes, which typically are observed from radiative non-Hermitian systems. Here we divert our attention to another new degree of freedom. We

find that it is possible to change the far-field properties of a topological interface state, since this extra degree of freedom is not dictated by the topological property. To the best of our knowledge, systems that can support such functionalities have not been investigated to date.

To validate these concepts, we have constructed a graphene Bragg grating of 20 unit cells. A domain wall in the center is created when two different sets of gate voltage are wired to the left or the right half of the grating. We explicitly prescribe the  $E_F(x)$  landscape across the grating using functions, for example, such as Eq. (4), or that calculated from the electrostatic simulation of  $E_F(x)$ . In the driven simulations, we employ focused Gaussian beams to excite this edge state, incident from different angles. In Figure 4C, we show the effective absorption cross-sectional spectra for varying incident angles. This edge mode exhibits a clearly anisotropic response. This is the result of the hybridization of bulk evanescent plasmon modes in the crystal bandgap; the even mode is horizontally polarized, and the odd mode is vertically polarized as a result of the free-charge distribution present on the

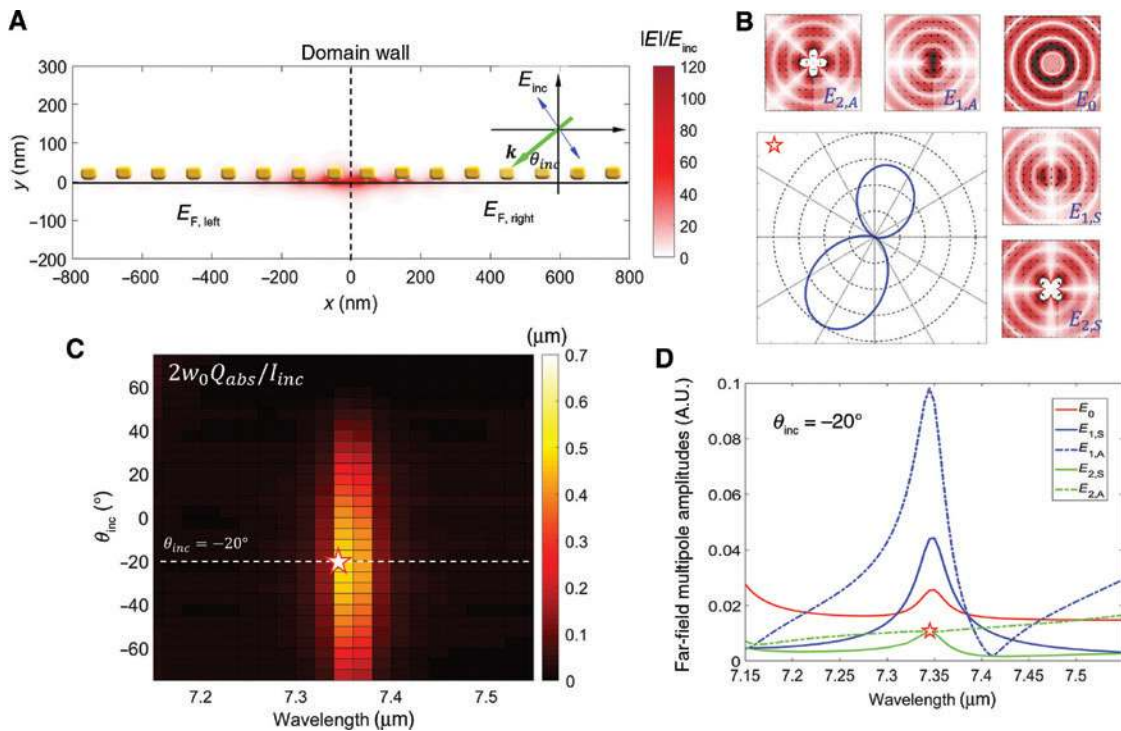


**Figure 4:** A GSSP SSH interface state.

(A) A model of graphene gratings with tunable band topologies on two sides of a domain wall. Coefficients of  $E_F$  functions Eq. (4) are explicitly prescribed.  $E_{F,\text{left}}$  (eV):  $E_F^{(0)} = 0.2$ ,  $E_F^{(1)} = -0.03$ ,  $E_F^{(2)} = -0.03$  and, for  $E_{F,\text{right}}$  (eV):  $E_F^{(0)} = 0.2$ ,  $E_F^{(1)} = 0.03$ ,  $E_F^{(2)} = 0.07$ . Only graphene and metal metagates are considered in the simulations. A Gaussian beam with waist size  $w_0 = 6 \mu\text{m}$  is p-polarized and its incident angle sweeps from  $-75^\circ$  to  $75^\circ$ . An edge-mode field enhancement is shown for incident angle  $-20^\circ$  at wavelength  $7.36 \mu\text{m}$ . (B) In the far-field, power flux is shown for the resonant edge mode excited by an  $-20^\circ$  incident light. Insets: electric field profile of quadrupole  $E_{2,A}$  and  $E_{2,S}$ , dipole  $E_{1,A}$  and  $E_{1,S}$ , and an out-of-plane magnetic mode  $E_0$ . Color represents their field amplitudes. (C) The color map shows effective absorption cross-section (1D) of the graphene grating. An edge mode is predicted by previous Zak phase analysis. Its spectral response, however, is not symmetric for incident light coming from opposite sides of the domain wall. (D) The edge mode far-field is expanded onto the multipole basis shown as insets in panel (B). Each mode amplitude is plotted as a function of wavelength for the  $-20^\circ$  incident case.

metal metagates. A comparison of the topological edge mode far-field with multipolar modes in Figure 4B and a multipole expansion in Figure 4D confirms the dominating presence of dipole moments as compared with weaker quadrupole and an out-of-plane magnetic moments. The localization of bulk evanescent modes can thus have an effect on the orientation of the mode. In the present model, the edge mode is highly localized and produces a small scattering cross-section under mid-IR illumination. The scattering effect can be improved by patterning unit cells with larger period, while a higher chemical potential is needed to offset the resonance red shift caused by a lower wave momentum according to Eq. (12). Then, an interesting possibility of manipulation of light with a high spatial localization and a tunable polarization can therefore be perceived by implementing this platform and benefit wave-steering applications.

Different from the graphene surface plasmon waveguide-like cavity mode, the 1D SSH edge state is robust against local perturbations near the domain wall. Although both can be spatially reconfigured by changing the gating voltage profile, the SSH edge state is resilient to a local perturbation in carrier density, which can result from fabrication imperfections of metagates, for example, a missing metal electrode. Instead, it is more likely to shift the cavity mode out of the bandgap. In fact, for small metagates as we have used in the present study, the size inhomogeneity can be a challenge for electrostatically reconfiguring the metasurface to arbitrarily move a cavity mode on the metasurface. To prospect future opportunities, the SSH edge state can be utilized in a large array or even stacked into multiple layers in order to increase the efficiency of a wave-steering application.

Nevertheless, the tunable reflectivity dips shown in Figures 3 and 4 can feature much narrower bandwidths ( $Q > 100$ ) compared to other active graphene-based mid-IR modulators such as graphene-integrated plasmonic metasurfaces ( $Q = 30$ ) [38–40, 48] or graphene nanodisk arrays ( $Q = 20$ ) [61]. This is because we utilize the high-quality, long-lived graphene plasmons [44, 65, 66] by avoiding the direct patterning of graphene. Therefore, supported by high tunability and sharp resonant responses, our proposed platform also promises potential applications for ultrafast and ultradense information encoders for mid-IR radiation.

## 5 Quantum nonlocality in graphene-integrated plasmonic structures

Finally, we will briefly discuss the nonlocal effects that occur with this system of Dirac fermions and its potential opportunities in this platform. In small plasmonic nanostructures, the key physical quantities that determine plasmonic resonance frequencies and the corresponding optical response, such as the electron conductivity or material permittivity, are more accurate using quantum mechanical or quasi-classical frameworks [67, 97–109]. For our current designs, which feature relatively large spacings between graphene and metagate contacts, the local carrier density profile is relatively smooth, i.e. contains a smaller contribution from the high-frequency spatial harmonics. Qualitative estimations [14, 67] suggest a relatively low degree of nonlocal effects that does not change the

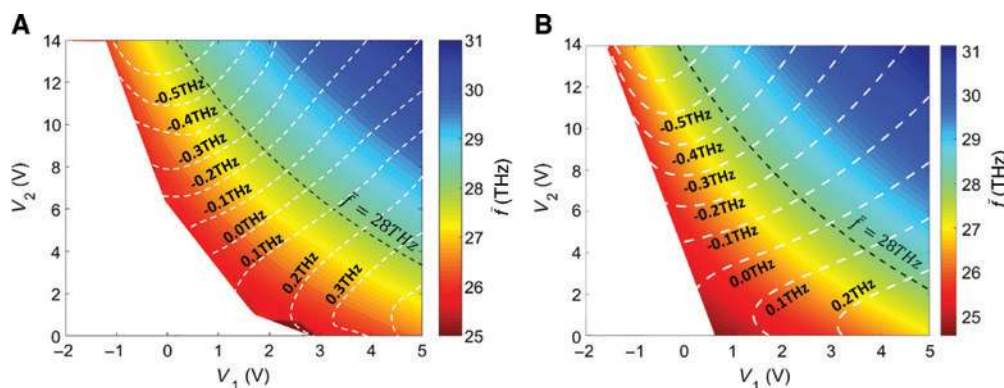


**Figure 5:** Comparison of band gap frequencies between local and non-local conductivity model.

(A) Using the conductivity equation [Eq. (2)] in COMSOL simulations, mid-gap frequencies  $\bar{f} = (f_{\text{odd}} + f_{\text{even}}) / 2$  are plotted in color as a function of top gate and back gate voltages. White dashed lines illustrate contours labeled with the bandgap size, defined as  $f_{\text{even}} - f_{\text{odd}}$ . (B) Same as (A), but using a nonlocal conductivity model [14]. In these simulations, the electrostatic gating was first solved, and the local carrier density is known. Then the infrared properties are simulated using the input carrier density for describing local or nonlocal response functions. The geometry would take the same template as shown in Figure 1A but without fillet features on metagates.  $w = 30$  nm and  $h = 6$  nm. Metal is treated as PEC in infrared property calculations. The electrostatic permittivity of hBN was taken from [110].

resonant frequency or band topology significantly. Nevertheless, the plasmonic structures with a stronger coupling between the Fourier components considered in this article represent a promising platform for future investigations of nonlocal effects of different quantum mechanical origins. Below we describe a simple model that captures the quantum mechanical nonlocality of electron-hole optical conductivity of graphene with nonuniform chemical potential.

For the noninteracting free carriers in graphene with inhomogeneous density, the following expression [14, 108] for the Hartree response has been suggested:

$$\chi_H(\mathbf{q}, \mathbf{q}', \omega) = \frac{\tilde{E}_F(\mathbf{q}-\mathbf{q}')}{\pi\hbar^2\omega^2} \mathbf{q} \cdot \mathbf{q}' - \frac{\tilde{E}_F^{-1}(\mathbf{q}-\mathbf{q}')}{4\pi} \mathbf{q} \cdot \mathbf{q}' + \frac{3v_F^2 \tilde{E}_F(\mathbf{q}-\mathbf{q}')}{4\pi\hbar^2\omega^2} (\mathbf{q} \cdot \mathbf{q}')^2. \quad (17)$$

For the system simulated in Figure 3, a quick estimate shows the following hierarchy of energy scales:  $\hbar\omega \approx 0.1$  eV,  $\hbar v_F |q| \approx 0.04$  eV, and  $\tilde{E}_F(0) \approx 0.3$  eV,  $\tilde{E}_F^{-1}(0) \approx 3.4$  eV<sup>-1</sup>,  $|\tilde{E}_F^{-1}(G)/\tilde{E}_F(G)| \approx 10$  eV<sup>-2</sup>,  $|\tilde{E}_F^{-1}(2G)/\tilde{E}_F(2G)| \approx 10$  eV<sup>-2</sup>, etc. Therefore, the magnitude of the second and third terms in Eq. (17) are small compared to the response because of a local conductivity equation [Eq. (2)], with the contribution of the third term being on the order of 10%. This impact on the graphene plasmon dispersions can be observed by comparing Figure 5A and B, where mid-gap frequency shifts by less than 5% for the same set of gate voltages. Overall, the contour lines resulting from the two models qualitatively resemble each other. These effects can be managed by more refined control of the gate voltages, as is observed in the comparison of simulations using local and nonlocal models in Figure 5A and B. Note that in this theoretical exploration, we have used rectangular-shaped metal stripes as top gates, so a sharper carrier density distribution may be expected. This allows us to observe a more profound nontrivial dependence of frequencies on local carrier densities designed by the local control of the gate voltages and device geometry, especially when contributions from higher momentum terms increase. As a final remark, it was also demonstrated that it discretizes the energies of the electronic states as a result of the high spatial confinement of the free carriers [77]. The characteristic energy may be on the order of 10 meV, estimated by a Dirac fermion-in-the-box model. It can potentially change the distribution of carriers and hence the optical conductivity [103, 104]. Therefore, the proposed graphene-integrated photonic platform can be employed in future studies of nonlocal quantum mechanical effects in graphene.

## 6 Conclusion

In this article, we have demonstrated a promising approach toward utilizing a double-gated graphene device for realizing a tunable plasmonic Bragg grating. The metal metasurface provides an interface for active and effective spatial modulation of local carrier densities, which mediates the hybridization of Bloch plasmonic modes and interacts directly with the GSPP modes in the infrared regime. We also showed that hBN, which provides protection against phonon scattering, mediates the decay factors of evanescent fields in different frequency regimes. The bandgap inversion was demonstrated in a transmission simulation, thus this inversion resulting in a switching of the Zak phase, as predicted by our theoretical calculations. An anisotropic edge state was found to exist between two such graphene Bragg gratings featuring different Zak phases. We predict that the orientation of the dipole moment can be tunable electrically, thereby making this a promising fundamental building block for ultrafast electro-optic devices. To design a useful device, however, it usually involves a multiphysics optimization which also takes into consideration the constraints resulting from imperfect fabrication as well as the exact material electrical and optical properties. Applications such as fast optical switches, tunable resonators or absorbers, and beam-steering devices can thus be perceived to benefit from this approach.

**Acknowledgments:** Funding support from the Office of Naval Research (Grant#N00014-17-1-2161), UDRI (Grant#RSC17004), the National Science Foundation (Grants No. DMR-1741788 and No. DMR-1719875), and the Army Research Office (Grant No. W911NF-16-1-0319) is acknowledged. M. J. acknowledges the support by the Kwanjeong Fellowship from the Kwanjeong Educational Foundation. J.A. and M.A. are thankful for support from AFOSR lab task 17RWCOR398 (PO: Dr K Caster), and S. T. thanks the AFRL and the NRC RAP fellowship for their support. S. I. would like to thank the ASEE fellowship and NRL for supporting this research work.

## References

- [1] Cheng X, Jouvaud C, Ni X, Mousavi SH, Genack AZ, Khanikaev AB. Robust reconfigurable electromagnetic pathways within a photonic topological insulator. *Nat Mater* 2016;15:542.
- [2] Hasan MZ, Kane CL. Colloquium: topological insulators. *Rev Mod Phys* 2010;82:3045–67.
- [3] Qi X-L, Zhang S-C. Topological insulators and superconductors. *Rev Mod Phys* 2011;83:1057–110.

- [4] Wang Z, Chong Y, Joannopoulos JD, Soljačić M. Observation of unidirectional backscattering-immune topological electromagnetic states. *Nature* 2009;461:772.
- [5] Khanikaev AB, Mousavi SH, Tse W-K, Kargarian M, MacDonald AH, Shvets G. Photonic topological insulators. *Nat Mater* 2012;12:233.
- [6] Lumer Y, Plotnik Y, Rechtsman MC, Segev M. Self-localized states in photonic topological insulators. *Phys Rev Lett* 2013;111:243905.
- [7] Hafezi M, Mittal S, Fan J, Migdall A, Taylor JM. Imaging topological edge states in silicon photonics. *Nat Photon* 2013;7:1001.
- [8] Lu L, Joannopoulos JD, Soljačić M. Topological photonics. *Nat Photon* 2014;8:821.
- [9] Wu L-H, Hu X. Scheme for achieving a topological photonic crystal by using dielectric material. *Phys Rev Lett* 2015;114:223901.
- [10] Ma T, Khanikaev AB, Mousavi SH, Shvets G. Guiding electromagnetic waves around sharp corners: topologically protected photonic transport in metawaveguides. *Phys Rev Lett* 2015;114:127401.
- [11] Lu L, Joannopoulos JD, Soljačić M. Topological states in photonic systems. *Nat Phys* 2016;12:626.
- [12] Gao F, Xue H, Yang Z, et al. Topologically protected refraction of robust kink states in valley photonic crystals. *Nat Phys* 2017;14:140.
- [13] Ma T, Shvets G. All-si valley-hall photonic topological insulator. *New J Phys* 2016;18:025012.
- [14] Jung M, Fan Z, Shvets G. Midinfrared plasmonic valleytronics in metagate-tuned graphene. *Phys Rev Lett* 2018;121:086807.
- [15] Su WP, Schrieffer JR, Heeger AJ. Solitons in polyacetylene. *Phys Rev Lett* 1979;42:1698–701.
- [16] Xiao M, Ma G, Yang Z, Sheng P, Zhang ZQ, Chan CT. Geometric phase and band inversion in periodic acoustic systems. *Nat Phys* 2015;11:240.
- [17] Zhao D, Xiao M, Ling CW, Chan CT, Fung KH. Topological interface modes in local resonant acoustic systems. *Phys Rev B* 2018;98:014110.
- [18] Meng Y, Wu X, Zhang R-Y, et al. Designing topological interface states in phononic crystals based on the full phase diagrams. *New J Phys* 2018;20:073032.
- [19] Longhi S. Zak phase of photons in optical waveguide lattices. *Opt Lett* 2013;38:3716–9.
- [20] Xiao M, Zhang ZQ, Chan CT. Surface impedance and bulk band geometric phases in one-dimensional systems. *Phys Rev X* 2014;4:021017.
- [21] Slobozhanyuk AP, Poddubny AN, Miroschnichenko AE, Belov PA, Kivshar YS. Subwavelength topological edge states in optically resonant dielectric structures. *Phys Rev Lett* 2015;114:123901.
- [22] Poddubny A, Miroschnichenko A, Slobozhanyuk A, Kivshar Y. Topological majorana states in zigzag chains of plasmonic nanoparticles. *ACS Photon* 2014;1:101–5.
- [23] St-Jean P, Goblot V, Galopin E, et al. Lasing in topological edge states of a one-dimensional lattice. *Nat Photon* 2017;11:651–6.
- [24] Abanin DA, Kitagawa T, Bloch I, Demler E. Interferometric approach to measuring band topology in 2d optical lattices. *Phys Rev Lett* 2013;110:165304.
- [25] Atala M, Aidelsburger M, Barreiro JT, et al. Direct measurement of the zak phase in topological bloch bands. *Nat Phys* 2013;9:795.
- [26] Zak J. Berry's phase for energy bands in solids. *Phys Rev Lett* 1989;62:2747–50.
- [27] Ryu S, Hatsugai Y. Topological origin of zero-energy edge states in particle-hole symmetric systems. *Phys Rev Lett* 2002;89:077002.
- [28] Li L, Xu Z, Chen S. Topological phases of generalized su-schrieffer-heeger models. *Phys Rev B* 2014;89:085111.
- [29] Yang Z, Gao F, Zhang B. Topological water wave states in a one-dimensional structure. *Sci Rep* 2016;6:29202.
- [30] Novoselov KS, Geim AK, Morozov SV, et al. Electric field effect in atomically thin carbon films. *Science* 2004;306:666–9.
- [31] Novoselov KS, Geim AK, Morozov SV, et al. Two-dimensional gas of massless dirac fermions in graphene. *Nature* 2005;438:197–200.
- [32] Novoselov KS, Jiang D, Schedin F, et al. Two-dimensional atomic crystals. *Proc Natl Acad Sci USA* 2005;102:10451–3.
- [33] Grigorenko AN, Polini M, Novoselov KS. Graphene plasmonics. *Nat Photon* 2012;6:749–58.
- [34] Koppens FHL, Chang DE, de Abajo FJG. Graphene plasmonics: a platform for strong light-matter interactions. *Nano Lett* 2011;11:3370–7.
- [35] Ju L, Geng B, Horng J, et al. Graphene plasmonics for tunable terahertz metamaterials. *Nat Nanotechnol* 2011;6:630–4.
- [36] Li Z, Yu N. Modulation of mid-infrared light using graphene-metal plasmonic antennas. *Appl Phys Lett* 2013;102:131108.
- [37] Chu H-S, Gan CH. Active plasmonic switching at mid-infrared wavelengths with graphene ribbon arrays. *Appl Phys Lett* 2013;102:231107.
- [38] Yao Y, Kats MA, Genevet P, et al. Broad electrical tuning of graphene-loaded plasmonic antennas. *Nano Lett* 2013;13:1257–64.
- [39] Dabidian N, Kholmanov I, Khanikaev AB, et al. Electrical switching of infrared light using graphene integration with plasmonic fano resonant metasurfaces. *ACS Photon* 2015;2:216–27.
- [40] Dabidian N, Dutta-Gupta S, Kholmanov I, et al. Experimental demonstration of phase modulation and motion sensing using graphene-integrated metasurfaces. *Nano Lett* 2016;16:3607–15.
- [41] Huidobro PA, Kraft M, Maier SA, Pendry JB. Graphene as a tunable anisotropic or isotropic plasmonic metasurface. *ACS Nano* 2016;10:5499–506.
- [42] Nikitin AY, González PA, Vélez S, et al. Real-space mapping of tailored sheet and edge plasmons in graphene nanoresonators. *Nat Photon* 2016;10:239–43.
- [43] Nikitin AY, Alonso-González P, Hillenbrand R. Efficient coupling of light to graphene plasmons by compressing surface polaritons with tapered bulk materials. *Nano Lett* 2014;14:2896–901.
- [44] Chen J, Badioli M, Alonso-Gonzalez P, et al. Optical nano-imaging of gate-tunable graphene plasmons. *Nature* 2012;487:77–81.
- [45] Velasco J, Ju L, Wong D, et al. Nanoscale control of rewriteable doping patterns in pristine graphene/boron nitride heterostructures. *Nano Lett* 2016;16:1620–5.
- [46] Ferrari AC, Bonaccorso F, Fal'ko V, et al. Science and technology roadmap for graphene, related two-dimensional crystals, and hybrid systems. *Nanoscale* 2015;7:4598–810.
- [47] Rodrigo D, Limaj O, Janner D, et al. Mid-infrared plasmonic biosensing with graphene. *Science* 2015;349:165–8.
- [48] Jung M, Dutta-Gupta S, Dabidian N, Brener I, Shcherbakov M, Shvets G. Polarimetry using graphene-integrated anisotropic metasurfaces. *ACS Photon* 2018;5:4283–8.
- [49] Yan H, Low T, Zhu W, et al. Damping pathways of mid-infrared plasmons in graphene nanostructures. *Nat Photon* 2013;7:394.

- [50] Alonso-González P, Nikitin AY, Golmar F, et al. Controlling graphene plasmons with resonant metal antennas and spatial conductivity patterns. *Science* 2014;344:1369–73.
- [51] Brar VW, Jang MS, Sherrott M, et al. Hybrid surface-phonon-plasmon polariton modes in graphene/monolayer h-bn heterostructures. *Nano Lett* 2014;14:3876–80.
- [52] Schiefele J, Pedrós J, Sols F, Calle F, Guinea F. Coupling light into graphene plasmons through surface acoustic waves. *Phys Rev Lett* 2013;111:237405.
- [53] Constant TJ, Hornett SM, Chang DE, Hendry E. All-optical generation of surface plasmons in graphene. *Nat Phys* 2015;12:124.
- [54] Dai S, Ma Q, Liu MK, et al. Graphene on hexagonal boron nitride as a tunable hyperbolic metamaterial. *Nat Nanotechnol* 2015;10:682.
- [55] Caldwell JD, Vurgafman I, Tischler JG, Glembocki OJ, Owrutsky JC, Reinecke TL. Atomic-scale photonic hybrids for mid-infrared and terahertz nanophotonics. *Nat Nanotechnol* 2016;11:9.
- [56] Caldwell JD, Novoselov KS. Mid-infrared nanophotonics. *Nat Mater* 2015;14:364.
- [57] Silveiro I, Manjavacas A, Thongrattanasiri S, de Abajo FJG. Plasmonic energy transfer in periodically doped graphene. *New J Phys* 2013;15:033042.
- [58] Jablan M, Buljan H, Soljačić M. Plasmonics in graphene at infrared frequencies. *Phys Rev B* 2009;80:245435.
- [59] Christensen J, Manjavacas A, Thongrattanasiri S, Koppens FHL, de Abajo FJG. Graphene plasmon waveguiding and hybridization in individual and paired nanoribbons. *ACS Nano* 2012;6:431–40.
- [60] Fang Z, Thongrattanasiri S, Schlather A, et al. Gated tunability and hybridization of localized plasmons in nanostructured graphene. *ACS Nano* 2013;7:2388–95.
- [61] Fang Z, Wang Y, Schlather AE, et al. Active tunable absorption enhancement with graphene nanodisk arrays. *Nano Lett* 2014;14:299–304.
- [62] Tassin P, Koschny T, Kafesaki M, Soukoulis CM. A comparison of graphene, superconductors and metals as conductors for metamaterials and plasmonics. *Nat Photon* 2012;6:259–64.
- [63] Woessner A, Lundeborg MB, Gao Y, et al. Highly confined low-loss plasmons in graphene–boron nitride heterostructures. *Nat Mater* 2014;14:421.
- [64] Thongrattanasiri S, Silveiro I, de Abajo FJG. Plasmons in electrostatically doped graphene. *Appl Phys Lett* 2012;100:201105.
- [65] Fei Z, Rodin AS, Andreev GO, et al. Gate-tuning of graphene plasmons revealed by infrared nano-imaging. *Nature* 2012;487:82.
- [66] Ni GX, McLeod AS, Sun Z, et al. Fundamental limits to graphene plasmonics. *Nature* 2018;557:530–3.
- [67] Woessner A, Gao Y, Torre I, et al. Electrical  $2\pi$  phase control of infrared light in a 350-nm footprint using graphene plasmons. *Nat Photon* 2017;11:421.
- [68] Forsythe C, Zhou X, Watanabe K, et al. Band structure engineering of 2d materials using patterned dielectric superlattices. *Nat Nanotechnol* 2018;13:566–71.
- [69] Geim AK, Novoselov KS. The rise of graphene. *Nat Mater* 2007;6:183–91.
- [70] Schwierz F. Graphene transistors. *Nat Nanotechnol* 2010;5:487–96.
- [71] Medina H, Lin Y-C, Oberfell D, Chiu P-W. Tuning of charge densities in graphene by molecule doping. *Adv Funct Mater* 2011;21:2687–92.
- [72] Craciun MF, Russo S, Yamamoto M, Tarucha S. Tuneable electronic properties in graphene. *Nano Today* 2011;6:42–60.
- [73] Kedzierski J, Hsu J P-L, Reina A, et al. Graphene-on-insulator transistors made using chemical-vapor deposition. *IEEE Electron Device Lett* 2009;30:7:745–7.
- [74] Cheianov VV, Fal'ko V, Altshuler BL. The focusing of electron flow and a veselago lens in graphene junctions. *Science* 2007;315:1252–5.
- [75] Shytov AV, Rudner MS, Levitov LS. Klein backscattering and fabry-pérot interference in graphene heterojunctions. *Phys Rev Lett* 2008;101:156804.
- [76] Zhao Y, Wyrick J, Natterer FD, et al. Creating and probing electron whispering-gallery modes in graphene. *Science* 2015;348:672–5.
- [77] Lee J, Wong D, Velasco J Jr, et al. Imaging electrostatically confined dirac fermions in graphene quantum dots. *Nat Phys* 2016;12:1032.
- [78] Jin D, Christensen T, Soljačić M, Fang NX, Lu L, Zhang X. Infrared topological plasmons in graphene. *Phys Rev Lett* 2017;118:245301.
- [79] Pan D, Yu R, Xu H, de Abajo FJG. Topologically protected dirac plasmons in a graphene superlattice. *Nat Commun* 2017;8:1243.
- [80] Forati E, Hanson GW, Yakovlev AB, Alú A. Planar hyperlens based on a modulated graphene monolayer. *Phys Rev B* 2014;89:081410.
- [81] Lu H, Zeng C, Zhang Q, et al. Graphene-based active slow surface plasmon polaritons. *Sci Rep* 2015;5:8443.
- [82] Tao J, Yu XC, Hu B, Dubrovkin A, Wang QJ. Graphene-based tunable plasmonic bragg reflector with a broad bandwidth. *Opt Lett* 2014;39:271–4.
- [83] Gao W, Shu J, Qiu C, Xu Q. Excitation of plasmonic waves in graphene by guided-mode resonances. *ACS Nano* 2012;6:7806–13.
- [84] Huidobro PA, Kraft M, Kun R, Maier SA, Pendry JB. Graphene, plasmons and transformation optics. *J Opt* 2016;18:044024.
- [85] Vakil A, Engheta N. Transformation optics using graphene. *Science* 2011;332:1291–4.
- [86] Liu M, Yin X, Ulin-Avila E, et al. A graphene-based broadband optical modulator. *Nature* 2011;474:64–7.
- [87] Falkovsky LA, Varlamov AA. Space-time dispersion of graphene conductivity. *Eur Phys J B* 2007;56:281–4.
- [88] Falkovsky LA, Pershoguba SS. Optical far-infrared properties of a graphene monolayer and multilayer. *Phys Rev B* 2007;76:153410.
- [89] Yu GL, Jalil R, Belle B, et al. Interaction phenomena in graphene seen through quantum capacitance. *Proc Natl Acad Sci* 2013;110:3282–6.
- [90] COMSOL AB. Comsol multiphysics® v. 5.4. www.comsol.com. Stockholm, Sweden, COMSOL AB, 2018. <https://www.comsol.com/support/knowledgebase/1223/>.
- [91] Caldwell JD, Kretinin AV, Chen Y, et al. Sub-diffractive volume-confined polaritons in the natural hyperbolic material hexagonal boron nitride. *Nat Commun* 2014;5:5221.
- [92] Pendry JB, Martn-Moreno L, Garcia-Vidal FJ. Mimicking surface plasmons with structured surfaces. *Science* 2004;305:847–8.
- [93] Dai S, Fei Z, Ma Q, et al. Tunable phonon polaritons in atomically thin van der waals crystals of boron nitride. *Science* 2014;343:1125–9.
- [94] Fefferman CL, Lee-Thorp JP, Weinstein MI. Topologically protected states in one-dimensional continuous systems and dirac points. *Proc Natl Acad Sci* 2014;111:8759–63.

- [95] Alonso-González P, Nikitin AY, Gao Y, et al. Acoustic terahertz graphene plasmons revealed by photocurrent nanoscopy. *Nat Nanotechnol* 2016;12:31.
- [96] Gorlach MA, Ni X, Smirnova DA, et al. Far-field probing of leaky topological states in all-dielectric metasurfaces. *Nat Commun* 2018;9:909.
- [97] Wang W, Kinaret JM. Plasmons in graphene nanoribbons: interband transitions and nonlocal effects. *Phys Rev B* 2013;87:195424.
- [98] Raza S, Toscano G, Jauho A-P, Wubs M, Mortensen NA. Unusual resonances in nanoplasmonic structures due to nonlocal response. *Phys Rev B* 2011;84:121412.
- [99] Fernández-Domnguez AI, Wiener A, Garca-Vidal FJ, Maier SA, Pendry JB. Transformation-optics description of nonlocal effects in plasmonic nanostructures. *Phys Rev Lett* 2012;108:106802.
- [100] McMahon JM, Gray SK, Schatz GC. Nonlocal optical response of metal nanostructures with arbitrary shape. *Phys Rev Lett* 2009;103:097403.
- [101] Torre I, Tomadin A, Geim AK, Polini M. Nonlocal transport and the hydrodynamic shear viscosity in graphene. *Phys Rev B* 2015;92:165433.
- [102] de Abajo FJG. Nonlocal effects in the plasmons of strongly interacting nanoparticles, dimers, and waveguides. *J Phys Chem C* 2008;112:17983–7.
- [103] Scholl JA, Koh AL, Dionne JA. Quantum plasmon resonances of individual metallic nanoparticles. *Nature* 2012;483:421.
- [104] Govorov AO, Zhang H, Gun'ko YK. Theory of photoinjection of hot plasmonic carriers from metal nanostructures into semiconductors and surface molecules. *J Phys Chem C* 2013;117:16616–31.
- [105] Esteban R, Borisov AG, Nordlander P, Aizpurua J. Bridging quantum and classical plasmonics with a quantum-corrected model. *Nat Commun* 2012;3:825.
- [106] Cirac C, Hill RT, Mock JJ, et al. Probing the ultimate limits of plasmonic enhancement. *Science* 2012;337:1072–4.
- [107] Cirac C, Pendry JB, Smith DR. Hydrodynamic model for plasmonics: a macroscopic approach to a microscopic problem. *Chem Phys Chem* 2013;14:1109–16.
- [108] Torre I, Katsnelson MI, Diaspro A, Pellegrini V, Polini M. Lippmann-schwinger theory for two-dimensional plasmon scattering. *Phys Rev B* 2017;96:035433.
- [109] Lundeberg MB, Gao Y, Asgari R, et al. Tuning quantum nonlocal effects in graphene plasmonics. *Science* 2017;357:187–91.
- [110] Cai Y, Zhang L, Zeng Q, Cheng L, Xu Y. Infrared reflectance spectrum of bn calculated from first principles. *Solid State Commun* 2007;141:262–6.